ADVANCING EARTH AND SPACE SCIENCES

Water Resources Research

RESEARCH ARTICLE

10.1029/2024WR038355

Key Points:

- The head loss due to two in-line logs decreased as the center-to-center log spacing decreased
- With log spacing greater than 10 times the log diameter, the hyporheic flows driven by each log did not interfere with each other
- Log-induced hyporheic flow has distinct patterns depending on the spacing between logs, similar to the surface flow patterns

Supporting Information:

Supporting Information may be found in the online version of this article.

Correspondence to:

J. Q. Yang,
judyyang@umn.edu

Citation:

Huang, S. H., Sawyer, A. H., Wohl, E., & Yang, J. Q. (2025). Flume experiments with refractive-index matched sediment revealing the impact of two in-line channel-spanning logs on hyporheic exchange. *Water Resources Research*, *61*, e2024WR038355. https://doi.org/10.1029/2024WR038355

Received 5 JUL 2024
Accepted 4 JUN 2025

Flume Experiments With Refractive-Index Matched Sediment Revealing the Impact of Two In-Line Channel-Spanning Logs on Hyporheic Exchange

S. H. Huang[1,2], **A. H. Sawyer**[3], **E. Wohl**[4], **and J. Q. Yang**[1,2]

[1]Saint Anthony Falls Laboratory, University of Minnesota, Minneapolis, MN, USA, [2]Department of Civil, Environmental, and Geo- Engineering, University of Minnesota, Minneapolis, MN, USA, [3]School of Earth Sciences, The Ohio State University, Columbus, OH, USA, [4]Department of Geosciences, Colorado State University, Fort Collins, CO, USA

Abstract In-channel wood, a critical component of forested rivers, has the capacity to enhance hyporheic flow. This process facilitates the continuous exchange of gases, solutes, and nutrients across the sediment-water interface, regulating pollutant transport and biogeochemical cycles in rivers. When two wood structures are in close proximity, the hyporheic flows induced by each log can interact, yet such effects remain largely uncharacterized. In this study, we investigated the impact of two in-line channel-spanning logs with a vertical gap above the sediment-water interface on hyporheic flow through laboratory experiments conducted under various conditions. Specifically, we measured water surface profiles, surface flow fields, and hyporheic flow fields around logs with different center-to-center distances (L_{c-c}). Our results demonstrated that when the center-to-center distance between two logs was less than 10 times the log diameter, the wakes of the two logs interfered with each other, resulting in a decrease in both hyporheic flow rates and the difference in water surface elevation. Furthermore, we demonstrated the relationship between the pattern of log-induced hyporheic flow and the surface flow regime. Our results suggest that the hyporheic flow pattern induced by logs can be inferred from measurements of the surface flow patterns. Our findings will contribute to an improved estimation of hyporheic flow induced by logs distributed along river channels.

Plain Language Summary Channel-spanning logs, large pieces of wood found in forested rivers, can slow down surface flow and drive hyporheic flow. Hyporheic flow, a bidirectional flow through the riverbed, retains nutrients and filters contaminants, thereby regulating river water quality. While the impact of a single channel-spanning log has been studied, the interaction between two closely spaced logs has not been well understood. In this study, we investigated the impact of two in-line channel-spanning logs on hyporheic flow through laboratory experiments with various distances between the logs. Our findings reveal that when the logs were close, their hyporheic flows interacted, resulting in a decrease in the total hyporheic flow rate. Additionally, we demonstrated that the patterns of hyporheic flow correlate with surface flow patterns, which can be easily visualized in the field using dyes. This correlation offers engineers a method to evaluate the interaction of log-induced hyporheic flows in natural settings based on surface flow patterns. Our findings contribute to a better estimation of hyporheic flow induced by scattered logs along river channels.

1. Introduction

In forested rivers and streams, in-stream large wood is ubiquitous and has a significant impact on water and sediment transport within the river corridor (Spreitzer et al., 2021; Wohl, 2016). Large wood has been observed to increase transient surface storage (Ader et al., 2021; Ensign & Doyle, 2005), sediment storage (Parker et al., 2017; Wohl & Scott, 2017), and the lateral connectivity between the main channel and flood plain (Keys et al., 2018; Sear et al., 2010). Moreover, in-stream large wood increases the abundance and diversity of habitat and food resources for fish and invertebrate fauna (Lester & Boulton, 2008; Nagayama & Nakamura, 2010). Consequently, wood placement and reintroduction of large wood in river corridors have been used as restoration techniques in recent years (Grabowski et al., 2019; Roni et al., 2015).

Furthermore, in-stream large wood has been known to enhance hyporheic flow (Ader et al., 2021; Doughty et al., 2020), which is the bidirectional flow across the sediment-water interface that carries surface water into the stream bed and then back to the surface (Boano et al., 2014; Gooseff, 2010). The hyporheic exchange of solutes (Marion et al., 2002; Stonedahl et al., 2012), gases (O'Connor & Hondzo, 2008; Tseng & Tinoco, 2022), nutrients

(Boulton et al., 1998; Schaper et al., 2019), and fine particles (Drummond et al., 2020; Packman et al., 2000; Yang, 2024) plays a critical role in regulating the biogeochemical cycle (Boano et al., 2010; Li et al., 2017) and determining pollutant fate (Jaeger et al., 2021; McCallum et al., 2020) within a river corridor.

The hyporheic flows induced by various large wood structures, such as wood steps (Endreny et al., 2011; Marston, 1982), single channel-spanning logs (Sawyer et al., 2011), porous log jams (Follett et al., 2020; Huang & Yang, 2023), and beaver dams (Janzen & Westbrook, 2011; Majerova et al., 2015), have been extensively studied. Here, we refer to log jams as accumulations of three or more pieces of large wood due to fluvial processes (Wohl & Scamardo, 2021). Endreny et al. (2011) quantified the hyporheic flow induced by a wood step. Sawyer et al. (2011, 2012) investigated the impact of single channel-spanning logs on hyporheic flow and heat exchange using both experimental and numerical simulations. Huang and Yang (2023), as well as Doughty et al. (2020), quantified the hyporheic flux induced by porous log jams in flume and field experiments, respectively. The hyporheic exchange induced by beaver dams has been examined based on field survey data (Janzen & Westbrook, 2011; Majerova et al., 2015). Although these studies focused on the impact of individual large wood structures on hyporheic flow, it is important to note that in forested rivers, large wood structures commonly occur in series (Ader et al., 2021; Zhang et al., 2020). Wilhelmsen et al. (2021) demonstrated that the hyporheic flow path could connect a series of log jams, suggesting more complex interactions among a series of large wood structures. To improve predictions of hyporheic flow in rivers with many wood logs, it is crucial to understand the collective impact of multiple large wood structures on the hyporheic flow.

Here, we investigated the hyporheic flow induced by two cylindrical channel-spanning logs placed at the same water depth under various conditions in a laboratory flume with transparent sediment. We placed the logs in the flume with a vertical gap above the sediment-water interface to simulate natural channel-spinning logs, where both ends are supported by the channel banks, leaving a gap between the log and the bed (Follett et al., 2021). Similar configurations have been used to investigate the impact of large wood on hyporheic flow and hydraulic resistance in previous studies (Hygelund & Manga, 2003; Sawyer et al., 2011; Wallerstein et al., 2002). In the presented work, we measured the water surface profiles and surface flow fields around logs with various center-to-center distances and at different locations under various mean flow rates. We visualized the log-induced hyporheic flow paths by tracking the movement of fluorescent dye in the transparent sediment and quantified the log-induced hyporheic flow rate and the length scale of hyporheic flow paths. We first quantified the hyporheic flow induced by a single log and then by two logs. Furthermore, we investigated the dependency of hyporheic flow on the center-to-center distance among two logs, the distance of the log from the sediment bed, and the flow rate. We discussed how our findings can contribute to improved estimation of hyporheic flow induced by logs scattering along river channels in future studies.

2. Background

Large wood, defined as fallen trees that are longer than one meter and with a diameter greater than 10 cm (Wohl et al., 2016), frequently accumulates in the middle of forested rivers. Large wood pieces can form various wood structures, such as wood steps, single channel-spanning logs, porous log jams, and woody dams. In nature, wood structures often occur in series (Ader et al., 2021; Zhang et al., 2020), yet few studies have explored the interactions of multiple structures. In this study, we investigated the impact of a series of channel-spanning wood logs on hyporheic flow in a gravel-bed stream with submerged logs placed perpendicular to the surface flow using flume experiments. Specifically, we simplified the flow past two in-line channel-spanning logs to the flow past two in-line circular cylinders, a phenomenon extensively studied over the past decades (Chen et al., 2020; Igarashi, 1984; Ozdil & Akilli, 2019). As the Reynolds number exceeds $Re_D = \overline{U}D/\nu = 40$, the flow separated from the edge of the log transitions to unsteady flow, and a von Kármán vortex street forms on the downstream side of the log. Here $\overline{U}$ is the streamwise mean surface flow velocity [m/s], D is the log diameter [m], and ν is the kinematic viscosity of water [m^2/s]. When there are two in-line logs, the flow separated from the upstream log interacts with the downstream log. The resulting flow structure depends on both the Reynolds number and the center-to-center spacing between the two in-line logs (L_{c-c}). When Re_D is around $10,000$, the surface flow exhibits three different patterns as L_{c-c} increases: extended-body regime, reattachment regime, and co-shedding regime (Sumner, 2010; Zhou & Yiu, 2006). When the center-to-center distance is small, specifically when $L_{c-c} < 2D$, the flow separates from the upstream log and passes over the downstream log, resulting in a surface flow field resembling that of a single bluff body. This phenomenon is referred to as the extended-body regime. As

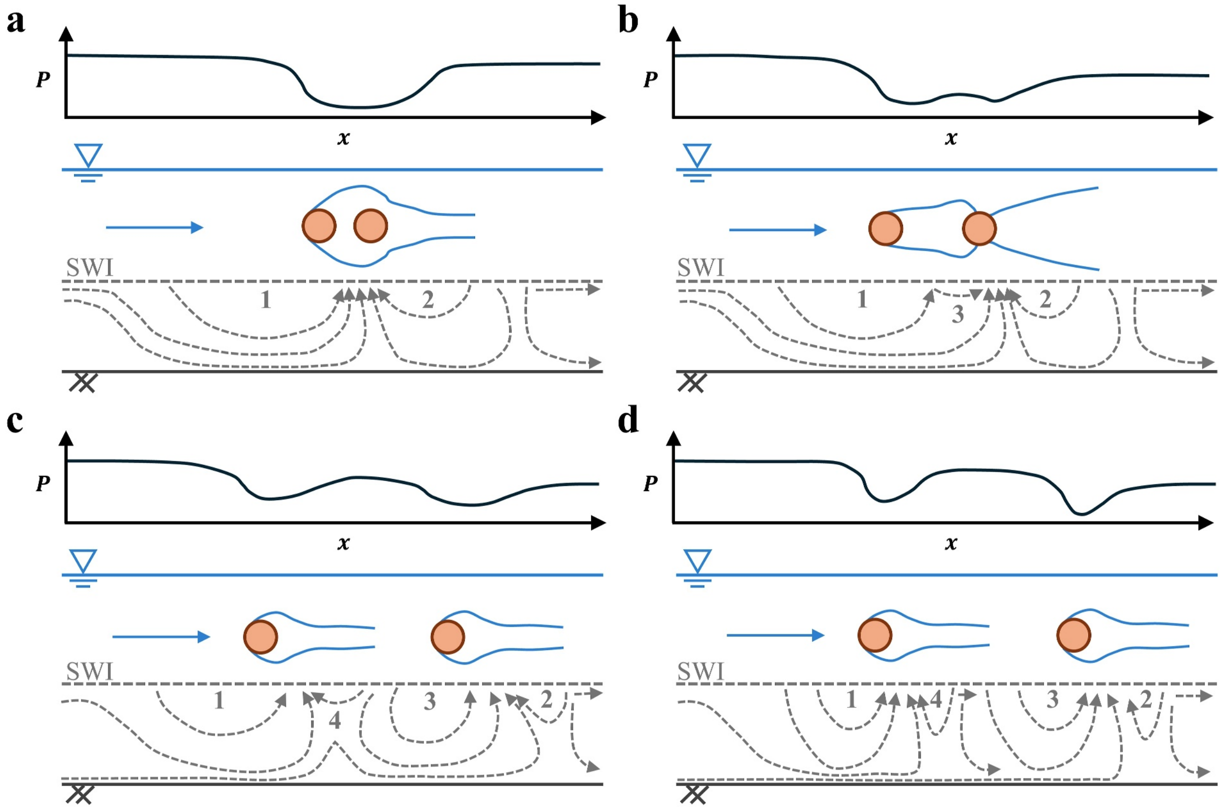

Figure 1. The pressure distribution at the sediment-water interface and the hyporheic flow pattern induced by two in-line logs at four different flow stages. (a) Stage I: Hyporheic flow upstream and downstream of the logs exits the sediment bed near the downstream log ($L_{c-c} < 2D$). (b) Stage II: A new location where surface flow enters the sediment appears between two logs ($2D \le L_{c-c} \le 4D$). (c) Stage III: A new region with a negative streamwise hyporheic flow velocity appears downstream of the upstream log. (d) Stage IV: The hyporheic flow is divided into two individual patterns. Numbers 1 to 4 indicate different bidirectional flow paths. *P* represents the pressure distribution at the sediment-water interface along the streamwise or *x*-direction for each stage.

the center-to-center distance increases to $2D \le L_{c-c} \le 4D$, the flow separated from the upstream log reattaches to the downstream log, which is referred to as the reattached regime. In this flow regime, various flow patterns have been observed between the logs, including synchronized flow, quasi-stationary vortex, vortex shedding, and bistable flow (Igarashi, 1984; Sumner, 2010). Finally, when the center-to-center distance further increases to $L_{c-c} \ge 4D$, a von Kármán vortex street is observed behind each log, a phenomenon referred to as the co-shedding regime. Note that the transition of L_{c-c} for each regime may be different at a different Reynolds number range (Sumner, 2010).

Despite these quantitative studies of the role of two in-line logs on surface flow, their impact on hyporheic flow has not been fully characterized. For a single channel-spanning log, previous studies have shown that the interaction of currents with the log and bed creates a zone of elevated hydraulic head beneath the upstream side of the log, followed by a drop in hydraulic head beneath the wake on the downstream side of the log, driving hyporheic flow (Sawyer et al., 2011). Hyporheic exchange rates are greatest beneath the log and decay roughly exponentially with distance upstream or downstream. For two in-line logs, the wake structures may interfere with each other and change the drag on the logs (Ljungkrona et al., 1991; Sumner, 2010), thereby altering the hydraulic head gradients at the sediment-water interface. Consequently, we anticipate that the hyporheic flow induced by the two in-line logs will differ from that induced by two individual logs, depending on the Reynolds number and the center-to-center spacing.

To address this knowledge gap, we propose that the hyporheic flow pattern induced by two in-line logs should change as L_{c-c} increases, resembling the patterns of the surface flow observed in previous studies (Igarashi, 1984; Sumner, 2010; Zhou & Yiu, 2006), as illustrated in Figure 1. First, when the two logs are positioned close to each other with $L_{c-c} < 2D$, we anticipate that the hyporheic flow pattern induced by the closely spaced logs should resemble that induced by a single log but be elongated. Specifically, we anticipate two bidirectional flows: one entering sediment from the upstream of the two logs and exiting at their downstream end (1 in Figure 1a), and another entering sediment from the downstream of the logs and exiting at the same downstream end (2 in Figure 1a). The two hyporheic flows mentioned above are induced by the pressure difference along the sediment-water interface, specifically between the high-pressure zone on both upstream and downstream sides of the logs and the low-pressure zone underneath the logs. According to Bernoulli's principle, as the flow approaches the logs, the pressure at the sediment-water interface first decreases due to increasing surface flow velocity, and then increases due to decreasing surface flow velocity. Accordingly, the pressure underneath the logs is lowest, leading to the two flow paths in the hyporheic zone. Second, as L_{c-c} increases to between $2D$ and $4D$, a third bidirectional flow enters and exits the sediment between two logs (3 in Figure 1b). Third, when $L_{c-c} > 4D$, we anticipate four bidirectional flow paths: two flow paths for each log (Figure 1c). The bidirectional flows between these two logs interfere with each other. Finally, when $L_{c-c} > 10D$, the hyporheic flow induced by the two logs should not interfere with each other (Figure 1d). One may use the relationship between the hyporheic flow patterns and the surface flow patterns proposed above to infer the hyporheic flow pattern based on the field's observed surface flow pattern, which is easily visible using visualization methods.

In addition to bi-directional hyporheic flow, logs can also regulate hyporheic exchange by generating near-bed turbulence, which is known to facilitate interfacial exchange by increasing the mechanical dispersion of solutes at the sediment-water interface (Roche et al., 2018; Voermans et al., 2018). In the following sections, we investigated how two in-line logs with varying center-to-center distances and the gaps between the log and sediment impact the bi-directional hyporheic flow and the near-bed turbulent kinetic energy through laboratory experiments.

3. Materials and Methods

The log experiments were conducted in a horizontal, straight water-recirculating channel in the Saint Anthony Falls Laboratory at the University of Minnesota. The smooth-wall channel was 12 m in length and 15 cm in width. A 6-meter test section with a permeable bed started three meters downstream of the inlet. The bottom of the test section was filled with a 15-cm-deep transparent porous bed, which was made of discrete spherical transparent hydrogel beads. The diameter of the hydrogel beads was $d_s = 5.6 \pm 0.6$ mm, and the porosity of the porous bed was $\phi_s = 0.3$ (Huang & Yang, 2022). The permeability estimated using the Karman-Cozeny relationship was $k = \phi_s^3 d_s^2 / 180 \left(1 - \phi_s\right)^2 = 9.6 \times 10^{-3}\ \mathrm{mm}^2$ (Voermans et al., 2018). The sediment hydraulic conductivity $K = k \rho g / \mu = 9.4\ \mathrm{cm/s}$. Here g was gravatiational accerleraction [$\mathrm{m/s^2}$], ρ was the water dentisty [$\mathrm{kg/m^3}$], and μ was the dynamic viscosity of water [$\mathrm{Pa \cdot s}$]. The hydraulic conductivity of the hydrogel beads tested in the current study corresponded to that of clear gravel, which typically ranges from 1 to 100 cm/s (Das, 2021). Four 1.5-m-long, 15-cm-wide plastic polyester meshes with 4 mm pores covered the beads to keep them from moving. The frames of the meshes were connected to each other by two 2-mm-diameter copper pins. The upstream and downstream boundaries of the porous bed were bounded by impermeable acrylic boards. The frames of the meshes were attached to the acrylic boards through copper pins. The surface water could only go into the sediment through the sediment-water interface in the test section. The outlet of the channel drained the water into a downstream tail tank. A valve at the end of the channel was used to control the flow rate through the outlet. The flow was pumped from the downstream tail tank to the inlet of the channel using a centrifugal pump. The bulk flow rate was measured using an orifice meter following the procedure proposed in ISO 5167-2:2003 (ISO, 2003). The setup of the orifice meter can be found in Text S1 in Supporting Information S1.

To simulate the impact of the individual logs on the flows, we simulated natural logs using plastic cylinders of 5 cm in diameter and placed them at various locations in the flume. To expand the plastic cylinders over the whole width of the flume, we cut them into two pieces (2 cm long and 12 cm long) and connected them together using a threaded rod (Figure 2a). This design allowed us to adjust the length of the plastic logs to fit tightly in the flume between the two side walls. The threaded rod should not impact the flow because we covered the whole plastic log (the two cylindrical pieces) with a 0.2-mm-thick plastic sheet and made the surface of the whole log smooth. Figure 2a shows the experimental setup. After the plastic logs were placed in the flume, we ran water through the flume using a centrifugal pump and adjusted the valve until the required water depth (H_{down}) reached 18 cm. The resulting blockage ratio was $B = D / H_{\mathrm{down}} = 0.28$. This value falls in the typical range of 0.28–0.67 observed in forested streams if the averaged water depth was 15–36 cm (Khosronejad et al., 2016; Manga & Kirchner, 2000)

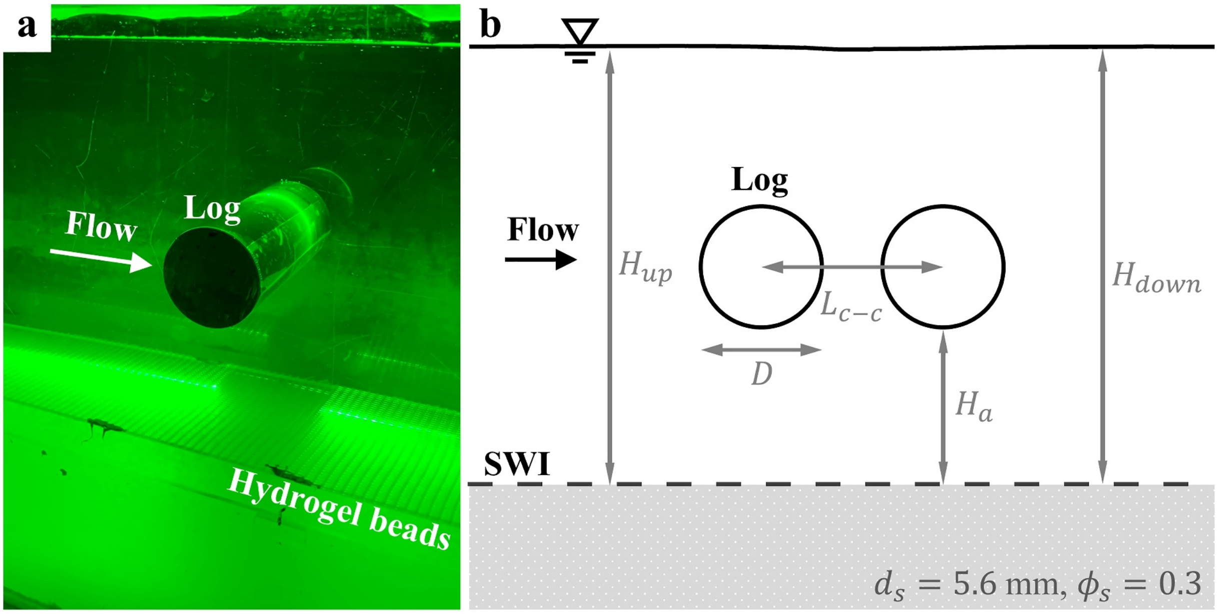

Figure 2. (a) Experimental setup. The log fitted tightly to the flume walls. The surface of the log was covered by a plastic sheet to make the surface smooth. (b) Definitions of the parameters used in the presented study. The blockage ratio is $B = D/H_{\text{down}}$, and the gap ratio is $G = H_a/H_{\text{down}}$. Here D is the log diameter [m]; H_{down} is the water depth [m]; H_a is the distance between the bottom of the log and the sediment-water interface [m]; and L_{c-c} is the horizontal center-to-center distance between two in-line logs [m]. Circles indicate the locations of the logs. The dashed line indicates the sediment-water interface. d_s is the sediment diameter, and ϕ_s is sediment porosity.

and log diameter was 10 cm. To account for different wood log placements relative to the riverbed, we tested three gap ratios, or the distance between the bottom of the plastic logs and the sediment-water interface (H_a) divided by the water depth, $G = H_a/H_{\text{down}} = 0.11$, 0.36, and 0.67 (Figure 2b) for submerged logs. The bulk flow rates measured using the orifice meter were 2.8, 3.8, 4.8, and 5.8 L/s. The corresponding flume Reynolds number was $Re_R = \overline{U}R/\nu = 6150$ to 12,200, consistent with the typical range of 1,000–129,600 for forested streams (Hart et al., 1999; Khosronejad et al., 2016; Manga & Kirchner, 2000). Here, R is the hydraulic radius of the channel [m]. For cases with two in-line logs, four center-to-center spacings $L_{c-c} = 1.5D, 3.0D, 6.0D$, and $10.0D$ were tested. The parameters for each test are listed in Table 1. We selected a log diameter of $D = 5$ cm due to the constraints of the channel depth. To scale our results to other log sizes, we normalized our results with log diameter. A previous study showed that the critical L_{c-c}, at which the surface flow changes its patterns, decreased with increasing blockage ratio (Jiang & Lin, 2012). In our study, the blockage ratio is a constant, so we anticipate that the trend of flow pattern developments will remain the same.

In addition to the bulk flow rates, the streamwise and vertical surface flow velocities near the plastic logs were measured using a customized 2D Particle Image Velocimetry (PIV). The PIV system consists of a 2-W green light laser at 532 nm wavelengths (LSR532F; Lasever, China) attached to a carriage and a side-looking camera with the maximum resolution of 1,224 × 1,024 pixels (BFS-U3-51S5M-C; FLIR Systems, Wilsonville). The carriage was manually moved in streamwise and spanwise directions. To measure the flow velocity, we seeded solid glass beads with a specific gravity of 2.6 and a mean diameter of 35 μm (3,000 E-Spheriglass; Potters Industries Inc., Pennsylvania). The seeding particles in the flow were illuminated with the 2-mm-thick laser sheet, and the pattern of the seeding particles was recorded by the side-looking camera for 90 s at 200 Hz. Finally, we calculated the flow velocity using the software PIVLab, developed by Thielicke and Sonntag (2021). To reduce the influence of the water surface vibrations on the location of the laser sheet, we placed an 8-cm-wide square plastic box on the water surface. Our results showed that the running average of instantaneous velocity converged within 90 s of measurement (Figure S1 in Supporting Information S1). We estimated the turbulent kinetic energy as $k_t = \frac{1}{2}\left(\overline{u'^2} + \overline{w'^2}\right)$, because our previous study suggests that the lateral velocity fluctuation is small and $\left(\overline{u'^2} + \overline{w'^2}\right)/\left(\overline{u'^2} + \overline{v'^2} + \overline{w'^2}\right) = 0.91 \pm 0.03$ around a pile of channel-spanning logs (Huang & Yang, 2023). Here, u' and w' represent the streamwise and vertical velocity fluctuations of the surface flow, respectively. To show the impact of the logs on the near-bed turbulence, we calculated k_t at 1 cm above the bed ($z = 1$ cm). For

Table 1
The Experimental Parameters

	Case no.	L_{c-c}/D[a]	Q [L/s]	$\overline{U}_{\text{up}}$ [cm/s]	G[b]	Setup no.
Cases with a log	SL-M-20 Hz	-	2.8	11.6	0.36	A
	SL-M-25 Hz	-	3.8	15.9	0.36	A
	SL-M-30 Hz	-	4.8	19.6	0.36	A/C
	SL-M-35 Hz	-	5.8	23.0	0.36	A
	SL-U-30 Hz	-	4.8	19.6	0.67	A
	SL-D-30 Hz	-	4.8	19.6	0.11	A
Cases with two logs	TL075-M-20 Hz	1.5	2.8	11.6	0.36	B
	TL150-M-20 Hz	3.0	2.8	11.6	0.36	B
	TL300-M-20 Hz	6.0	2.8	11.6	0.36	B
	TL500-M-20 Hz	10.0	2.8	11.6	0.36	B
	TL075-M-30 Hz	1.5	4.8	19.6	0.36	B/C
	TL150-M-30 Hz	3.0	4.8	19.6	0.36	B/C
	TL300-M-30 Hz	6.0	4.8	19.6	0.36	B/C
	TL500-M-30 Hz	10.0	4.8	19.6	0.36	B/C
	TL300-U-30 Hz	6.0	4.8	19.6	0.67	B
	TL300-D-30 Hz	6.0	4.8	19.6	0.11	B

[a] Log diameter $D = 5$ cm. [b] Gap ratio $G = H_a/H_{\text{down}}$.

reference, this height was about two sediment grain diameters and was chosen because the PIV measurements had large errors within 1 cm of the bed. The methods used to process the near-bed k_t can be found in Text S2 in Supporting Information S1. The spatially averaged $\overline{k}_t$ was the near-bed k_t averaged over the region from 30 cm upstream to 30 cm downstream of the logs, where the vertical hyporheic flux was calculated (see details below).

We measured water surface profiles around the log by illuminating the water surface with scattered laser light and recording the location of the water surface with a side-looking camera (D7500; Nikon, Japan). The water surface that reflected the laser light was bright compared to the background, which made the water surface easily detectable using the "edge" function in MATLAB (Canny, 1986). The water surface was measured for 30 s at 60 Hz, and the temporally averaged water surface elevations near the plastic logs were calculated. The water surface profile above the logs was noisy due to the reflection of the logs, thus, the profile in the region with logs is not presented. To investigate the energy loss of the surface flow caused by the logs, we estimated the head loss of the surface flow (h_L) due to the logs by comparing the hydraulic head (h) 15 cm upstream of the upstream log and 30 cm downstream of the downstream log. Here, $h = h_e + H + \overline{U}^2/2g$; h_e is the elevation head [m]; H is the water depth [m]; and g is the gravitational acceleration [m/s^2].

Furthermore, we measured the log-induced hyporheic flow velocity through dye visualization experiments. Specifically, we injected 0.5 mL of 0.005 wt% fluorescent dye (Fluorescein sodium salt, Sigma-Aldrich F6377) into the porous bed at around 30 to 100 points at the center of the channel ($y = 7.5$ cm). We stimulated the dye with blue light using a 30 cm × 30 cm LED array and made the dye emit green light. The location and shape of the dye plume over time were recorded by a side-looking camera (D7500; Nikon, Japan) with a green light filter (FGV9S; Thorlabs, Newton) at 60 Hz. We detected the boundaries of the dye plume on each image based on an intensity threshold determined by the contrast of the image intensity. Afterward, the hyporheic flow velocity was calculated as the difference in the centroid of the dye plume divided by the time interval. Based on hyporheic flow velocity, we calculated the vertical hyporheic flux per unit width of the channel by integrating the downward vertical dye migration velocity across the horizontal sediment layer, namely $q_H = \int_{x_{\text{log,down}}+30\text{ cm}}^{x_{\text{log,up}}-30\text{ cm}} |W_{\text{dye},c}(x)| f(x) \phi_s dx$ at $z = -2.5$ cm. Here $f(x) = \begin{cases} 1, \text{if } W_{\text{dye},c}(x) \le 0 \\ 0, \text{if } W_{\text{dye},c}(x) > 0 \end{cases}$, and ϕ_s was the sediment porosity. Downward velocity was chosen because upward-moving dye quickly diffused into the surface water, making it difficult to track. The depth of

$z = -2.5$ cm was selected because it was the closest location to the sediment-water interface where dye could be reliably tracked. For each case, we integrated the flux from 30 cm upstream to 30 cm downstream of the logs, where the depth-averaged streamwise hyporheic flow velocity was similar to the value of the case without logs. We normalized q_H by sediment hydraulic conductivity K and log diameter D.

Three series of experiments were conducted: A (11/1/2023–12/2/2023), B (1/18/2024–3/19/2024), and C (4/22/2024–5/23/2024). For each series, the hydrogel beads made from polysaccharides (Ma et al., 2019) were slightly different in shape and size as some of the beads were replaced due to microbial contamination. The difference in the measured q_H between Series B and Series C for the case with same L_{c-c} was shown in Figure S3 in Supporting Information S1. The mean and standard deviation of the difference $\Delta q_H/q_H = \frac{|q_{H,B} - q_{H,C}|}{q_{H,C}} \times 100$ [%] for cases with $L_{c-c}/D = 1.5, 3.0, 6.0, 10.0$ were 24% and 27%, respectively. The difference in q_H had a large mean and standard deviation because $\Delta q_H/q_H = 63\%$ for the cases with $L_{c-c}/D = 6.0$. We compared data from experiments in the same series, so the variations in hyporheic flux due to the replacement of the hydrogel beads would not affect our conclusions.

Finally, to quantify the length scale of the log-induced hyporheic flow, we defined the upstream hyporheic flow cell length ($L_{H,\mathrm{up}}$) and downstream hyporheic flow cell length ($L_{H,\mathrm{down}}$). $L_{H,\mathrm{up}}$ was the maximum horizontal distance between the point where surface flow on the upstream side of the upstream log entered the sediment and the point where it exited. Similary, $L_{H,\mathrm{down}}$ was the maximum horizontal distance between the point where surface flow on the downstream side of the downstream log entered the sediment and the point where it exited.

4. Results

4.1. The Impact of In-Line Channel-Spanning Logs on Surface Flow

To investigate the impact of two in-line logs on the surface flow, we measured the instantaneous flow velocity near the logs along a vertical (x-z) plane in the middle of the channel width ($y = 7.5$ cm) using a 2-dimensional (2D) PIV. The time-averaged streamwise flow velocity for single log cases with different Q is plotted by color in Figure S4 in Supporting Information S1. The resulting depth-averaged streamwise flow velocity one meter upstream of the log was $\overline{U}_{\mathrm{up}} = 11.6, 15.9, 19.6,$ and 23.0 cm/s, respectively. The Reynolds number based on the log diameter was $Re_D = \overline{U}_{\mathrm{up}} D/\nu = 5800, 7950, 9800$ and 11500, respectively. The flow pattern was similar across the different flow rates considered in this study; therefore, we focused on two flow rates, $Q = 2.8$ and 4.8 L/s, for two log cases.

For two log cases with flow rate $Q = 4.8$ L/s, the depth-averaged streamwise flow velocity one meter upstream of the two logs measured using PIV was $\overline{U}_{\mathrm{up}} = 19.6 \pm 0.3$ cm/s ($Re_D = \overline{U}_{\mathrm{up}} D/\nu \approx 9800$). The time-averaged streamwise flow velocity for cases with different L_{c-c} is plotted by color in Figure 3. As shown in Figure 3, when L_{c-c} increased, the surface flow exhibited three different patterns: extended-body regime, reattachment regime, and co-shedding regime (Sumner, 2010; Zhou & Yiu, 2006). Specifically, when the center-to-center distance was small, that is, $L_{c-c} = 1.5D$, the flow separated from the upstream log passed the downstream log, and the surface flow field resembled that of a single bluff body (Figure 3b), which was referred to as the extended-body regime. As the center-to-center distance increased to $L_{c-c} = 3D$, the surface flow pattern fluctuated between two states intermittently: one where the flow separated from the upstream log and reattached to the downstream log, and another where von Kármán vortex street shedding from the upstream log (Figure 3c). The abovementioned flow is constant with the bistable flow behavior defined in Section 2. According to the classification in the previous literature, it was referred to as the reattached regime (Sumner, 2010). Finally, when the center-to-center distance further increased to $L_{c-c} \geq 6D$, a von Kármán vortex street was observed behind each log, and this behavior was referred to as the co-shedding regime (Figures 3d and 3e). The results of the cases with $Q = 2.8$ L/s show a similar trend (Figure S5 in Supporting Information S1).

To further understand the impact of surface flow on hyporheic exchange, we plotted the time-averaged streamwise flow velocities closest to the sediment-water interface ($z = 1$ cm) in the mid-channel width ($y = 7.5$ cm) as a function of the streamwise location. To compare the flow velocity in the single log cases across various flow rates, we normalized the streamwise velocity using the mean surface flow velocity measured one meter upstream of the log, that is, $U_{x,z=1\text{ cm}}/\overline{U}_{\mathrm{up}}$. For all the velocities considered in this study ($\overline{U}_{\mathrm{up}} = 11.6$ cm/s to 23.0 cm/s, $Re_D = 5800$ to 11500), the near-bed streamwise surface flow velocity first increased as the flow

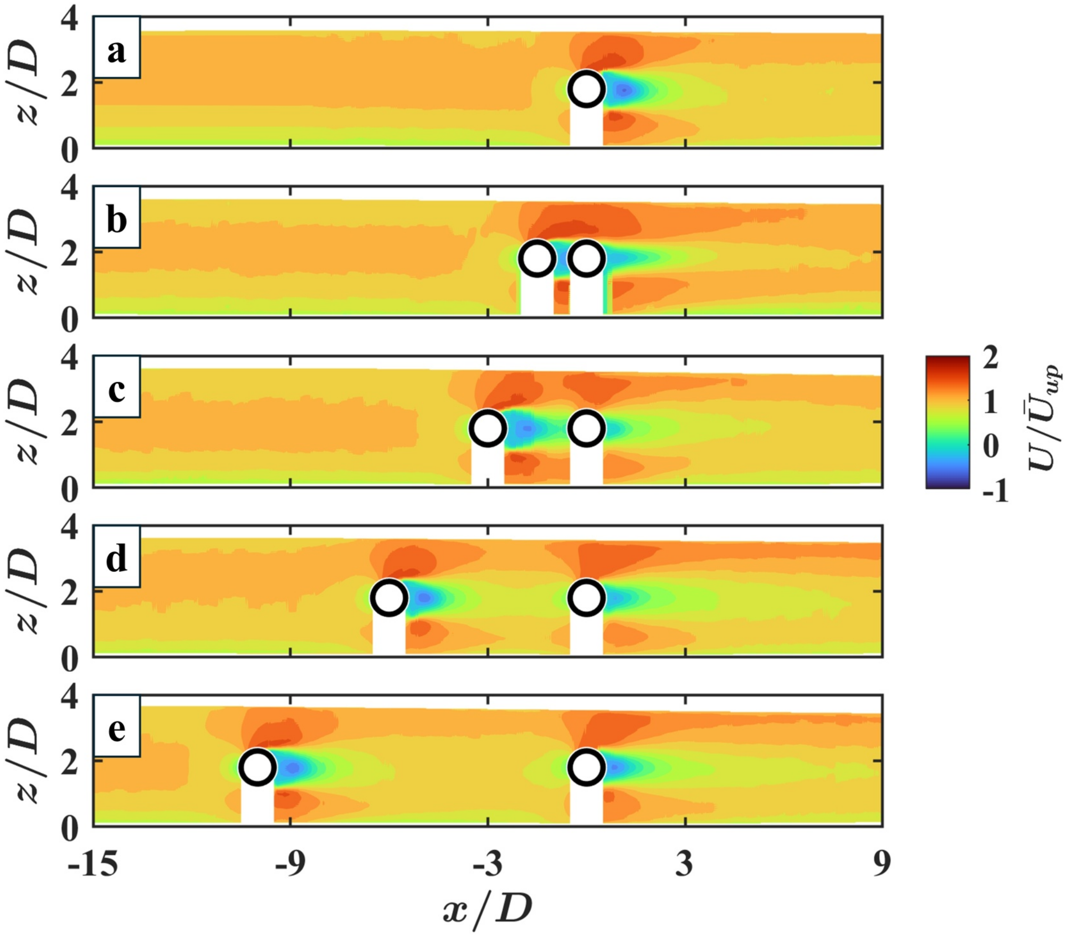

Figure 3. Time-averaged streamwise surface flow velocity for cases with different center-to-center distances L_{c-c} between two in-line logs. The mean streamwise surface flow velocity one meter upstream of the logs was $\overline{U}_{\mathrm{up}} = 19.6 \pm 0.3$ cm/s for all cases. (a) Case with a single log. (b) $L_{c-c} = 1.5D$. (c) $L_{c-c} = 3.0D$. (d) $L_{c-c} = 6.0D$. (e) $L_{c-c} = 10.0D$. $D = 5.0$ cm. Black open circles represent the channel-spanning logs. The flow was from left to right. The blank regions below the logs do not have flow velocity measurements because the laser was blocked by the logs.

approached the log, reaching its maximum magnitude on the downstream side of the log, and then decreased to a value about 1.2 times the upstream flow velocity, as shown in Figure S6 in Supporting Information S1. To compare the velocity in different cases with two logs, we plotted the x-axis as the location relative to the center of the upstream log in the streamwise direction. Figure 4 shows the results for cases with a flow rate of $Q = 4.8$ L/s ($\overline{U}_{\mathrm{up}} = 19.6$ cm/s, $Re_D = 9800$). The streamwise surface flow velocity first increased as the surface flow approached the upstream log and then decreased until the flow encountered another log. Our results show that when $L_{c-c} \leq 3D$, the flow reached its maximum velocity between two in-line logs. In contrast, when $L_{c-c} \geq 6D$, two peaks of the streamwise velocity were observed, and the surface flow reached its maximum magnitude on the downstream side of each log. Based on Bernoulli's principle, the pressure at the sediment-water interface decreases with increasing surface flow velocity. Therefore, we anticipated that the exit locations of the hyporheic flow correspond to the regions with the highest near-bed surface flow velocity, and the lowest pressure.

In addition to altering the mean surface flow velocity, the logs also affect the near-bed turbulent kinetic energy k_t (Figure 5a and Figure S2 in Supporting Information S1). The near-bed k_t on the downstream side of the log gradually increased along the streamwise direction and reached a plateau 20 cm downstream of the log (Figure 5a). Figure 5b shows the spatially averaged near-bed turbulent kinetic energy $\overline{k}_t$ for cases with different L_{c-c} at $\overline{U}_{\mathrm{up}} = 19.6 \pm 0.3$ cm/s. At the same mean streamwise surface flow velocity, $\overline{k}_t$ in a channel with logs was twice as high as $\overline{k}_t$ in a channel without logs (Figure 5b). In addition, $\overline{k}_t$ increased by almost two times when L_{c-c} was larger

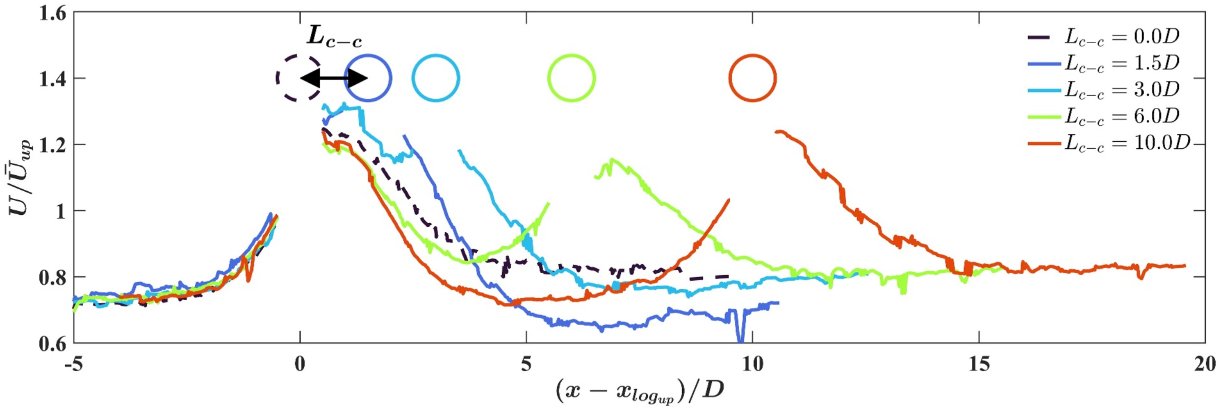

Figure 4. The time-averaged streamwise surface flow velocity near the sediment-water interface, namely at $z = 1$ cm, for cases with different center-to-center distances L_{c-c} between the two in-line logs. The mean streamwise surface flow velocity one meter upstream of the logs was $\overline{U}_{\text{up}} = 19.6 \pm 0.3$ cm/s for all cases. The x-axis represents the streamwise location relative to the center of the upstream log $x_{\text{log}_{\text{up}}}$. The black dashed open circle represents the location of the upstream log, and the open circles of other colors represent the streamwise locations of the downstream log placed at varying locations. The color of the curves echoes the color of the log. The regions without flow velocity measurement were the regions occupied by the logs. The dashed black curve with $L_{c-c} = 0.0D$ represents the case with a single log. $D = 5.0$ cm.

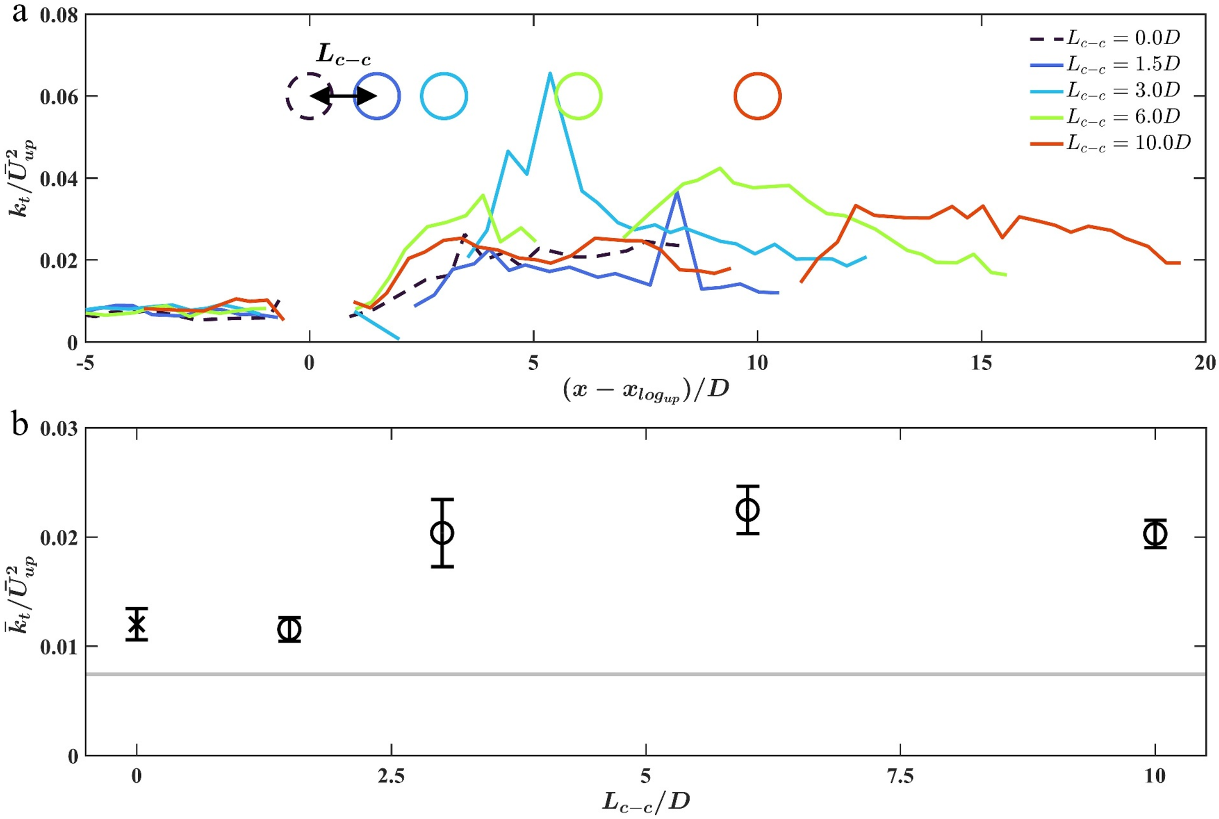

Figure 5. (a) The near-bed turbulent kinetic energy $k_t = \frac{1}{2}(\overline{u'}^2 + \overline{w'}^2)$ along the streamwise direction for cases with different center-to-center distances L_{c-c}. The x-axis represents the streamwise location relative to the center of the upstream log $x_{\text{log}_{\text{up}}}$. The black dashed open circle represents the location of the upstream log, and the open circles of other colors represent the streamwise locations of the downstream log placed at varying locations. The color of the curves echoes the color of the log. The regions without measurement were the regions occupied by the logs. The dashed black curve with $L_{c-c} = 0.0D$ represents the case with a single log. (b) Spatially-averaged turbulent kinetic energy $\overline{k}_t$ near the sediment-water interface, specifically at $z = 1$ cm, for cases with different center-to-center distances L_{c-c}. Cross marker represents $\overline{k}_t$ of a single log. Open circles represent the $\overline{k}_t$ of two in-line logs. The error bars show the range of $\overline{k}_t$ with one standard error. The gray patch shows the range of $\overline{k}_t$ with one standard error in a channel without logs. The mean streamwise surface flow velocity one meter upstream of the logs was $\overline{U}_{\text{up}} = 19.6 \pm 0.3$ cm/s for all cases. The log diameter $D = 5.0$ cm.

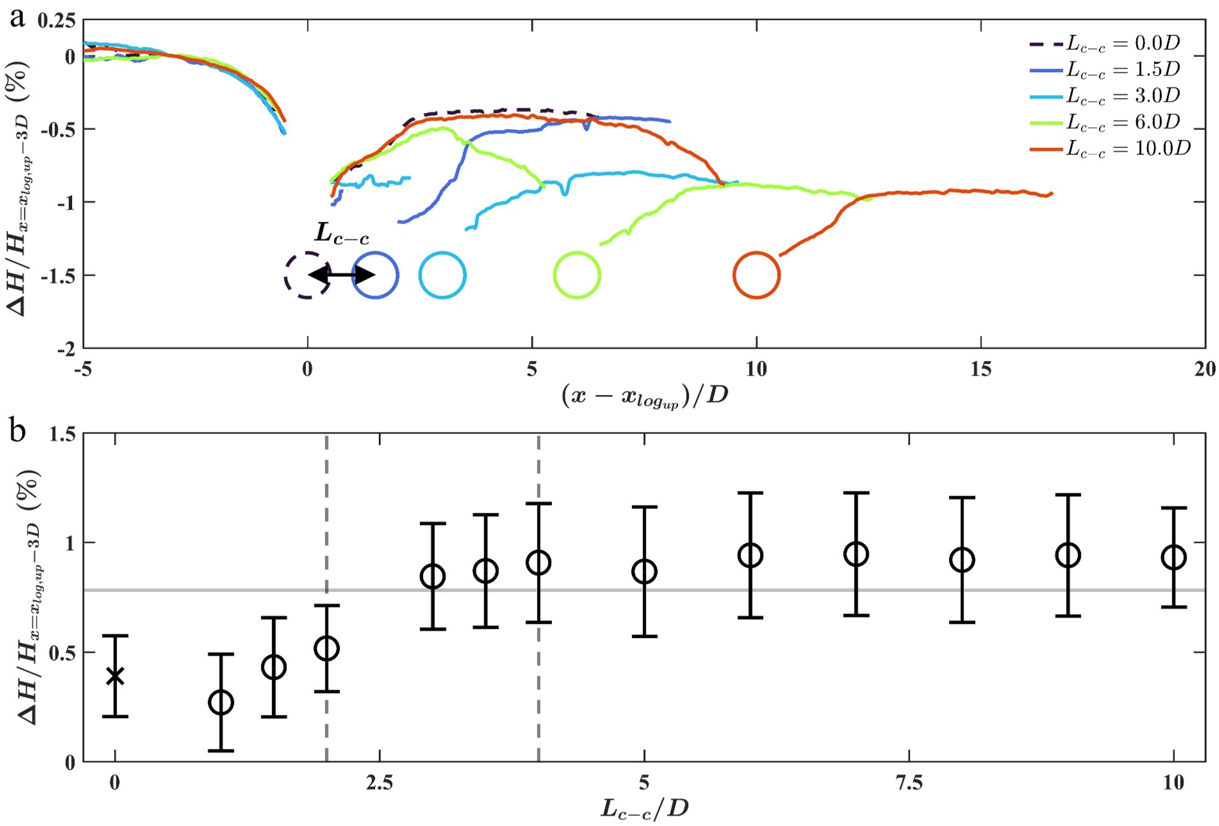

Figure 6. (a) The relative water surface profiles for cases with different center-to-center distances L_{c-c}. The x-axis represents the streamwise location relative to the center of the upstream log $x_{\log_{\rm up}}$. The black dashed open circle represents the location of the upstream log, and the open circles of other colors represent the streamwise locations of the downstream log placed at varying locations. The color of the curves echoes the color of the log. The regions without measurement were the regions occupied by the logs. The dashed black curve with $L_{c-c} = 0.0D$ represents the case with a single log. (b) The normalized difference in water depth between 15 cm upstream of the upstream log and 30 cm downstream of the downstream log. The cross marker represents the water surface difference of a single log. Open circles represent the water surface difference of two in-line logs with various center-to-center distances. The gray horizontal line indicates two times the water difference of a single log. Vertical dashed lines indicate $L_{c-c}/D = 2$ and 4, respectively. The log diameter $D = 5.0$ cm. The mean streamwise surface flow velocity one meter upstream of the logs was $\overline{U}_{up} = 19.6 \pm 0.3$ cm/s for all cases. The reference water surface elevation was 15 cm upstream of the upstream log.

than $3D$, compared with closely-spaced logs ($L_{c-c} = 1.5D$). $\overline{k}_t$ for the cases with $\overline{U}_{\rm up} = 11.6 \pm 0.3$ cm/s show a similar trend to $\overline{k}_t$ for the cases with $\overline{U}_{\rm up} = 19.6 \pm 0.3$ cm/s (Figure S7 in Supporting Information S1). The increase in near-bed turbulent kinetic energy will further facilitate the exchange of mass and momentum across the sediment-water interface (Voermans et al., 2018).

4.2. The Impact of In-Line Channel-Spanning Logs on Water Surface Profile

In addition to the surface flow velocity, we recorded the water surface profile using a laser light and a side-looking camera. For comparison, we calculated the relative water depth as the absolute water depth minus the reference water depth at 15 cm upstream of the first log, that is, $\Delta H(x) = H(x) - H_{x=x_{\rm log,up}-3D}$. As shown in Figure 6a, when $L_{c-c} \leq 3D$, the water surface elevation first decreased as the surface flow approached the log, reaching its minimum elevation on the downstream side of the log, and then increased to a stable elevation. In contrast, when the center-to-center distance $L_{c-c} \geq 6D$, the water surface elevation increased after the surface flow passed the upstream log and then decreased again as the surface flow approached the downstream log. Figure 6b shows the normalized difference in the water surface elevation, comparing measurements taken 15 cm upstream of the upstream log to those taken 30 cm downstream of the downstream log across different L_{c-c}. When $L_{c-c} \leq 3D$, the water surface difference for the case with two in-line logs was between one to two times the water surface difference for the case with a single log, suggesting that the water surface profiles induced by the two logs interfered with each other when $L_{c-c} \leq 3D$. As L_{c-c} increased, the water surface difference increased until it reached a plateau, or two times the water surface difference of the single log case, at $L_{c-c} > 5D$, suggesting that the interference of the two logs was small at $L_{c-c} > 5D$.

4.3. The Impact of In-Line Channel-Spanning Logs on Hyporheic Flow

To investigate how a sequence of logs impacts hyporheic flow, we conducted dye visualization experiments with two logs in the flume and analyzed the hyporheic flow paths induced by the two in-line logs with four center-to-center distances, $L_{c-c} = 1.5D, 3D, 6D$, and $10D$. The log-induced hyporheic flows were visualized by a green, fluorescent dye, as shown in Figures 7b–7e, respectively. Our results show that when $L_{c-c} = 1.5D$, the pattern of the combined hyporheic flow induced by the two in-line logs resembled the hyporheic flow induced by a single log, though elongated. Specifically, the hyporheic flows upstream and downstream of the two logs moved toward the downstream log (Figure 7b), similar to the pattern of a single log (Figure 7a). It suggests that the hyporheic flow induced by two closely spaced logs can be approximated as the hyporheic flow induced by a single bluff body, as depicted by the Stage I pattern in Figure 1. For the case of $L_{c-c} = 3D$, the hyporheic flow pattern was bistable, namely, the flow pattern switched between two patterns periodically, which was similar to the surface flow. The first pattern, which was shown in Figure S8a in Supporting Information S1, was similar to the Stage I pattern in Figure 1. On the other hand, as shown in Figures 7c and Figure S8b in Supporting Information S1, the second pattern was similar to the Stage II pattern in Figure 1, in which the surface flow entered the sediment at the sediment-water interface between the two in-line logs. For the case with $L_{c-c} = 6D$, the hyporheic flow pattern of each of the two logs resembled that of an individual structure. Two hyporheic flow fields interacted with each other, consistent with the Stage III pattern in Figure 1. Finally, when L_{c-c} was $10D$, the pattern of the hyporheic flow induced by each log was similar to the pattern of a single log (Figure 7e and Figure S9 in Supporting Information S1), as depicted by the Stage IV pattern in Figure 1. Our results suggest that the hyporheic flow induced by each log did not interact with each other and could be treated separately when $L_{c-c} \geq 10D$.

Further, from the hydproheic flow paths, we quantified the length scale of the log-induced hyporheic flow, that is, the upstream and downstream hyporheic flow cell lengths $L_{H,\mathrm{up}}$ and $L_{H,\mathrm{down}}$, respectively (Figure 7a). At $U_{\mathrm{up}} = 19.6 \pm 0.3$ cm/s, for cases with $L_{c-c} = 0D, 1.5D, 3D, 6D$, and $10D$, $L_{H,\mathrm{up}} = 44$ cm, 46 cm, 54 cm, 79 cm, and 92 cm, respectively, while $L_{H,\mathrm{down}} = 16$ cm, 34 cm, 15 cm, 16 cm, and 16 cm, respectively. Our results show that $L_{H,\mathrm{up}}$ increased by two times as L_{c-c} increased from $0D$ to $10D$. In contrast, $L_{H,\mathrm{down}}$ first increased by twofold when L_{c-c} increased from $0D$ to $1.5D$ and then decreased to the value of a single log as L_{c-c} further increased.

Finally, we calculated the vertical hyporheic flow flux per unit channel width (q_H) (see Methods for details). For both the cases with $\overline{U}_{\mathrm{up}} = 11.6 \pm 0.3$ cm/s (Figure S10 in Supporting Information S1) and $\overline{U}_{\mathrm{up}} = 19.6 \pm 0.3$ cm/s (Figure 8), q_H increased with increasing L_{c-c}. For the cases with $\overline{U}_{\mathrm{up}} = 19.6 \pm 0.3$ cm/s, the hyporheic flow rate induced by two in-line logs reached two times that of a single log when $L_{c-c} \geq 10D$ (Figure 8), suggesting that the interactions between two logs decreased the total log-induced hyporheic flow when $L_{c-c} < 10D$.

5. Discussions

5.1. The Change of the Surface and Hyporheic Flow Behaviors With Log Spacing

In previous studies, the pattern of the surface flow past two in-line logs was classified into three main regimes as L_{c-c} increased: the extended-body regime, the reattachment regime, and the co-shedding regime. For surface flow, the magnitude of the peak near-bed k_t was closely related to the surface flow pattern (Figure 5a). Specifically, when the two logs were close ($L_{c-c} = 1.5D$) and the surface flow was in the extended-body regime, with the measured peak k_t smaller than of a single log. When $L_{c-c} = 3D$, the surface flow entered the reattachment regime, and the strong interaction between the wakes of two logs leads to a peak k_t higher than of a single log. As $L_{c-c} = 6D$, the interaction between the wakes of two logs became weaker, leading to a smaller peak k_t than in the case with $L_{c-c} = 3D$. As the distance between two logs further increased, the interaction between the wakes of two logs continue to weaken, and the peak k_t generated by each log resembled the peak k_t of a single log.

Changes of $\overline{k}_t$, ΔH, and h with increasing L_{c-c} show a similar trend. Specifically, compared with the case of single log, $\overline{k}_t$, ΔH, and h first decreased at $L_{c-c} = 1.5D$, dramatically increased at $L_{c-c} = 3D$, and then gradually increased with increasing L_{c-c} (Figures 5b, 6b, and 9b). Our results demonstrate that when the surface flow

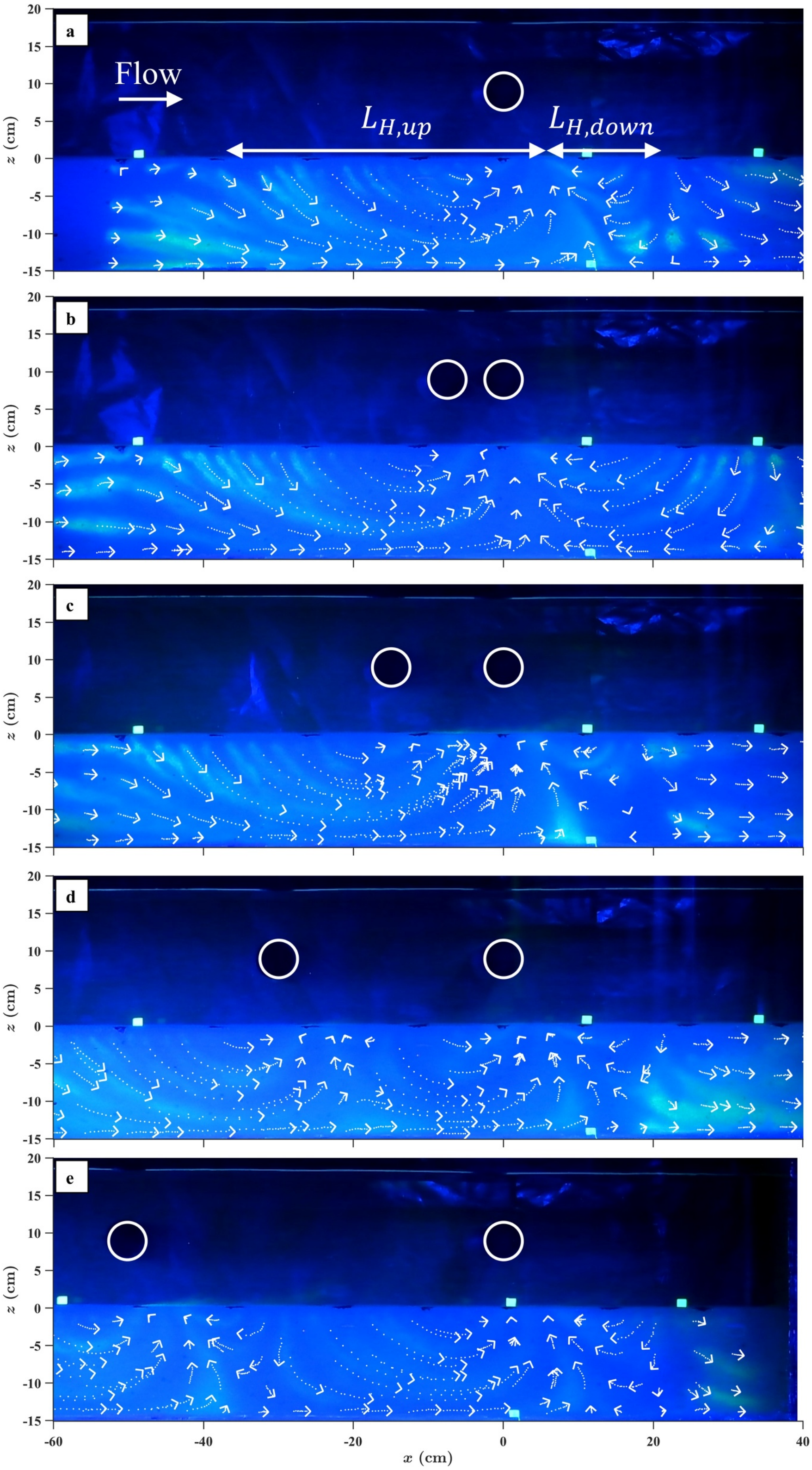

Figure 7.

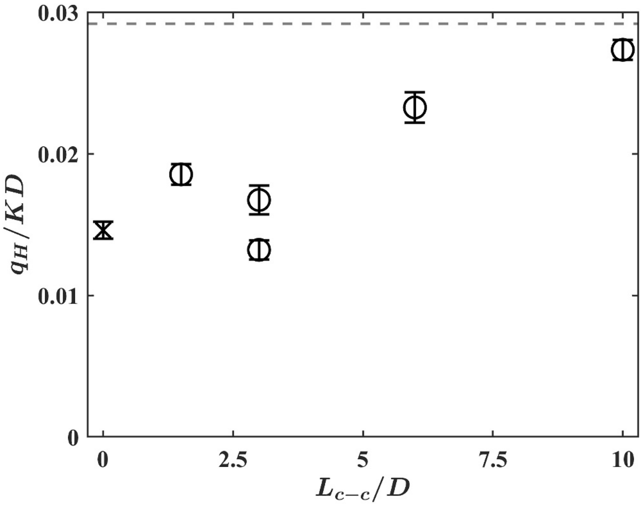

Figure 8. The hyporheic flow flux per unit channel width for cases with different center-to-center distances between two in-line logs L_{c-c}/D at $z = -2.5$ cm. The cross symbol represents the hyporheic flow rate of a single log. Open circles represent the hyporheic flow rate of two in-line logs. The gray horizontal line indicates two times the hyporheic flow rate of a single log. The mean streamwise surface flow velocity one meter upstream of the logs was $\overline{U}_{\text{up}} = 19.6 \pm 0.3$ cm/s for all cases. Log diameter $D = 5$ cm. Sediment hydraulic conductivity $K = 9.4$ cm/s.

passing the two in-line logs interacted ($L_{c-c} < 10D$), the head loss due to the logs was less than two times the head loss of a single log (Figure 9b). This observation implies that the energy loss of the surface flow caused by two logs was smaller than the total energy loss of the surface flow caused by two logs individually due to wake interference. This could lead to a smaller hydraulic head gradient along the bed.

Regarding hyporheic flow behavior, our results indicate that the hyporheic flow pattern varies according to the center-to-center distance (L_{c-c}), closely resembling the surface flow patterns. First, when $L_{c-c} < 3D$, the hyporheic flow pattern was in the Stage I regime, related to the surface flow in both the extended-body regime and reattachment regime (Figure 1a). When $L_{c-c} = 3D$, with the surface flow exhibiting bistability, which the surface flow was in the reattachment regime, the hyporheic flow pattern transitioned periodically between the Stage I and Stage II regimes (Figure 1b). When the hyporheic flow pattern was in Stage I, q_H was higher (Figure 8), which was consistent with the fact that q_H for the case with $L_{c-c} = 1.5D$ was higher than in the case with $L_{c-c} = 3D$. When $3D < L_{c-c} < 10D$, with the surface flow in the co-shedding regime, the hyporheic flow pattern was in the Stage III regime. Here, each log exhibited a hyporheic pattern akin to that of a single log, albeit with variations in size and magnitude (Figure 1c). Finally, when L_{c-c} exceeds $10D$, the hyporheic flow pattern entered Stage IV, where the hyporheic flow induced by the two logs exhibited minimum interference with each other (Figure 1d). Figure 9 summarizes typical surface and hyporheic flow patterns with various log center-to-center spacing at $Re_D = 9800$.

Our results showed that the development of the log-induced hyporheic flow patterns was related to the wake inference of the surface flow around the logs. The behavior of the surface flow around the logs has been extensively studied in the past decades (Chen et al., 2020; Igarashi, 1984) and can be readily observed using visualization methods. The relationship we propose here can be used to infer the hyporheic flow pattern based on the observed surface flow pattern in the field.

5.2. The Length Scale and Flow Rate of the Hyporheic Flow Induced by Two In-Line Logs

Regarding the length scale of the log-induced hyporheic flow, the upstream hyporheic flow cell length $L_{H,\text{up}}$ increased with increasing L_{c-c} (Figure 9c). Specifically, our results show that the upstream hyporheic flow cell length of a single log ($L_{H,\text{up},s}$) was 44 cm. The relative distance between the most upstream location at which the surface flow entered the sediment and the upstream log remained constant with increasing L_{c-c}. This is likely because that the water surface and streamwise velocity profiles in the streamwise direction at the upstream side of the upstream log were similar across all cases (Figures 4 and 6a). As a result, the hydraulic head gradients upstream the logs were similar, and the hyporheic flows on the upstream side had similar lengths. In addition, for the case with $L_{c-c} = 1.5D$, the upstream hyporheic flow exited the sediment between two logs (Figure 7b). As a result, $L_{H,\text{up}} < L_{H,\text{up},s} + L_{c-c}$. In contrast, for case with $L_{c-c} \geq 3D$, there was a hyporheic flow path connecting the regions between two logs, and the upstream hyporheic flow cell length can be approximated as the sum of the upstream hyporheic flow cell length of a single log and the center-to-center distance, namely $L_{H,\text{up}} \approx L_{H,\text{up},s} + L_{c-c}$.

On the other hand, the downstream hyporheic flow cell length $L_{H,\text{down}}$ with $L_{c-c} = 1.5D$ was two times that of a single log. For the cases with surface flow in both the reattachment regime and the co-shedding regime (cases with $L_{c-c} \geq 3D$), $L_{H,\text{down}} = 16$ cm was similar to $L_{H,\text{down}}$ for the case with a single log (Figure 9d). For the case with

Figure 7. The hyporheic flow induced by two in-line logs with various center-to-center distances between these two logs: (a) Case with a single log; (b) $L_{c-c} = 1.5D$; (c) $L_{c-c} = 3.0D$; (d) $L_{c-c} = 6.0D$; (e) $L_{c-c} = 10.0D$. $D = 5.0$ cm. The surface flow was from left to right. The mean streamwise surface flow velocity one meter upstream of the log was $U_{\text{up}} = 19.6 \pm 0.3$ cm/s for all cases. The white circles represent the locations of the logs. The green color shows the location of the fluorescent dye and was used to map the log-induced hyporheic flow path. White dashed curves with arrows indicate the path and the direction of the hyporheic flow identified from the dye injection experiments.

10.1029/2024WR038355

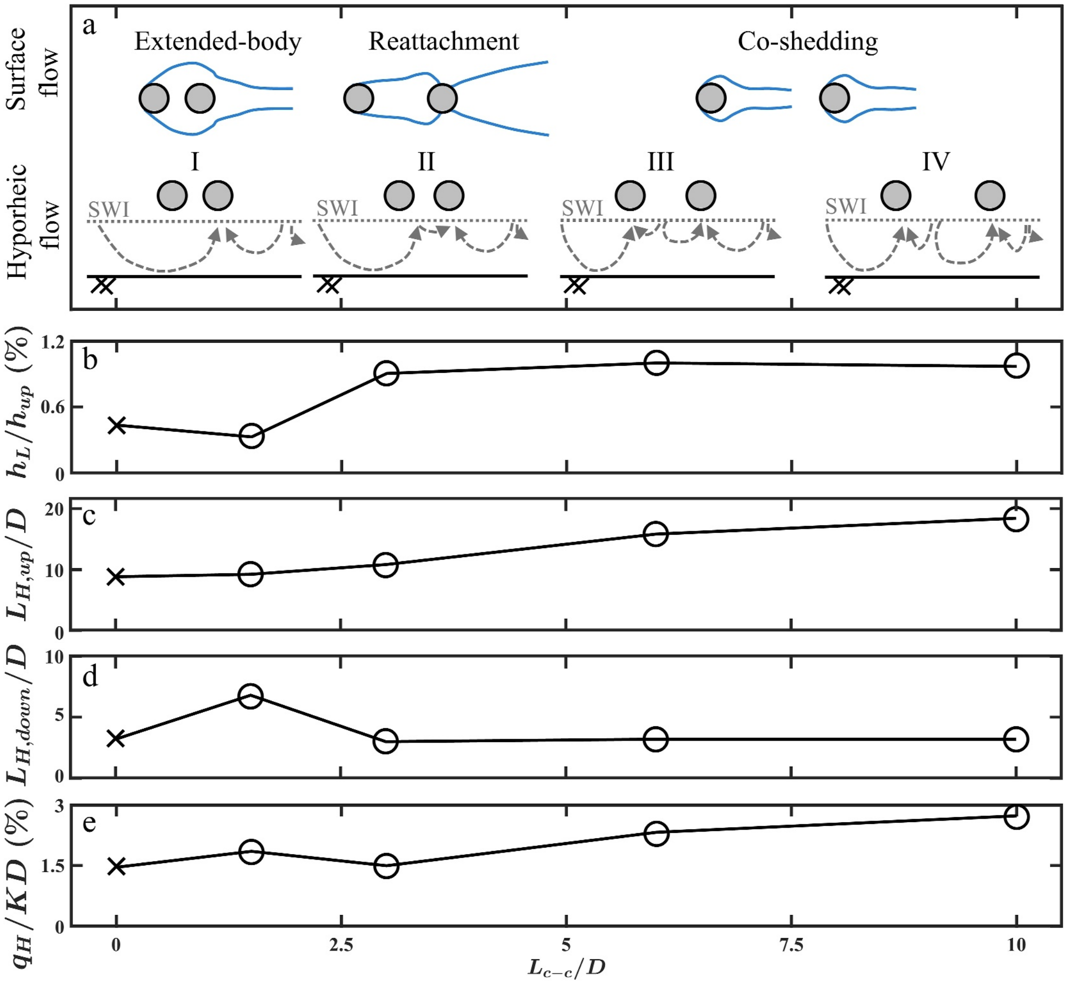

Figure 9. Flow parameters at different center-to-center distances L_{c-c} at $Re_D = 9800$. (a) Surface and hyporheic flow patterns with various log center-to-center spacing. (b) Head loss due to the logs. (c) Upstream hyporheic flow cell length normalized by log diameter. (d) Downstream hyporheic flow cell length normalized by log diameter. (e) Downward hyporheic flux per unit channel width. The cross symbol represents the parameters of a single log. Open circles represent the parameters of two in-line logs.

$L_{c-c} = 1.5D$, the region of high surface flow velocity extended further downstream (Figure 3b), resulting in a longer downstream hyporheic flow path. In contrast, for cases with $L_{c-c} \geq 3D$, the development of surface flow past the downstream log was similar to that observed with a single log (Figures 3a, 3c, 3d, and 3e). As a result, $L_{H,\text{down}}$ was similar among these cases.

Regarding the log-induced hyporheic flow rates, compared with single log cases, q_H first increased at $L_{c-c} = 1.5D$ and exhibited bistability at $L_{c-c} = 3D$. For cases with $L_{c-c} > 3D$, q_H gradually increased with increasing L_{c-c}. Finally, q_H for the two-log case reached about twice of q_H for a single log at $L_{c-c} = 10D$.

Our results show that the hyporheic flux induced by two logs was less than two times the hyporheic flux of a single log when $L_{c-c} < 10D$. In comparison, when the center-to-center distance $L_{c-c} \geq 10D$, the hyporheic flow flux induced by two in-line logs could be roughly estimated as twice the flux of a single log. Consequently, the hyporheic exchange facilitated by each log could be assessed independently.

Hyporheic flow regulates mass and thermal exchange in the sediment bed (Sawyer et al., 2012; Swanson & Cardenas, 2010). With the same number of logs in the channel, the shorter the hyporheic flow cell length induced by each log, the higher the spatial heterogeneity of temperature, nutrients, and oxygen distributed in the sediment bed. The increasing complexity of the habitat strengthens the resilience of the ecosystem (Wohl, 2016). Our results suggest that to maximize log-induced hyporheic flow rate, engineers and managers should introduce the logs into the channel with spacings greater than 10 times the log diameter. Our results show that when the logs were placed in the middle of the water column, the wake interference length decreased by $1D$ when Re_D increased from 5,800 to 9,800 (Figure 3c and Figure S5c in Supporting Information S1), consistent with the previous wind tunnel experiments, which show that the wake interference length decreased with increasing Re_D (Igarashi, 1984; Sumner, 2010). As a result, we anticipated that the recommended log spacings may decrease with increasing Re_D. In contrast, when the logs were placed near the sediment-water interface and water surface, the length in which the wake interference significantly increased (see Section 5.3). Furthermore, while we normalized q_H with sediment hydraulic conductivity K and log diameter D, we anticipate that q_H/DK may increase when sediment size d_s and D increased. This is because an increase in d_s may induce additional grain-scale hyporheic flow due to the roughness element (protruding sediment particles) on the channel bed. An increase in D can also lead to a larger blockage ratio, which would increase the resistance of the log to the flow (Manga & Kirchner, 2000) and increase the log-induced hyporheic flow rate (Sawyer et al., 2011).

Note that our results provide guidance for future use of logs in remediation of pollutants from the perspective of hyporheic flow rates, including recommendations on log spacing to increase the residence time of pollutants in the sediment of artificial wetlands for more effective biodegradation. Guidance on the other aspects, such as habitat complexity and ecosystem resilience, requires further investigations.

Finally, we demonstrated that the log-generated turbulence reached the channel bed (Figure 5a), which could facilitate the transfer of mass and momentum across the sediment-water interface (Roche et al., 2018; Voermans et al., 2018). Current studies predict the turbulence-induced interfical exchange rate using fluid viscosity, sediment permeability, and surface flow properties such as shear velocity and near-bed turbulent kinetic energy (O'Connor & Harvey, 2008; Voermans et al., 2018). However, when groundwater discharge is present in the channel, the interfacial exchange rate deviates from the rate predicted based only on the surface flow properties (O'Connor & Harvey, 2008). Our results demonstrated that the regions impacted by the near-bed log-generated turbulence overlapped with the regions affected by the log-induced hyporheic flow (Figure S11 in Supporting Information S1). Both the temporal and spatial scales of the exchange induced by log-induced hyporheic flow and near-bed log-generated turbulence are different. How logs impact the overall hyporheic exchange rate requires further investigation.

5.3. The Impact of the Gap Ratio on the Surface and Hyporheic Flows

In addition to varying flow velocity and log spacing, we adjusted the vertical location of the logs to $z = 4.5, 9.0$, and 14.5 cm to examine the effect of the gap ratio on the surface flow and hyporheic exchange. The corresponding gap ratios were $G = H_a/H_{\mathrm{down}} = 0.11, 0.36$, and 0.67, respectively. Here, H_a was the distance between the logs and the sediment-water interface, and H_{down} was the water depth 1 m downstream of the logs. Both single log cases and two log cases were considered. The center-to-center distance between the two logs was $L_{c-c} = 30$ cm ($6D$) for all the cases, and the depth-averaged streamwise flow velocity at one meter upstream of the logs was maintained at $\overline{U}_{\mathrm{up}} = 19.6 \pm 0.3$ cm/s. As shown in the surface flow field measured using a PIV (Figure S12 in Supporting Information S1), at the same mean streamwise surface flow velocity, the spatial heterogeneity of the streamwise surface velocity was higher when the logs were placed near the water surface or the sediment bed compared to when they were placed in the middle of the water column.

The log-induced water depth difference was higher when the logs were placed near the water surface or sediment bed (Figure S13 in Supporting Information S1). In addition, the near-bed turbulent kinetic energy was higher when the log was placed near the sediment bed (Figure S14 in Supporting Information S1). In contrast, the maximum k_t in the surface water column decreased when the logs were placed near the water surface or the sediment-water interface compared to when they were placed in the middle of the water column.

Furthermore, we compared our turbulent kinetic energy measurements with previous studies using different setups. In our study, $k_t/\overline{U}_{\mathrm{up}}^2$ in the surface flow for the log placed in the middle of the water column ($z = 9.0$ cm) in our experiment was up to 0.3. Our results are consistent with Schalko et al. (2021), which shows that for cases with a submerged log placed at the bottom of the channel, the maximum $k_t/\overline{U}_{\mathrm{up}}^2 = 0.2$. For emergent log with log emerged from the water surface, the maximum $k_t/\overline{U}_{\mathrm{up}}^2 = 1.2$ in Schalko et al. (2021), much larger than the maximum value in our setup. These results suggest that whether the logs were emergent or not may have a greater impact on the log-induced k_t than the gap ratio. In addition, in our experiment, the log-induced increase in k_t was first observed on the downstream side of the log and gradually extended to the water surface and sediment-water interface in the further downstream region (Figure S2 in Supporting Information S1). However, for the case of a channel-spanning log jam with a vertical gap, Müller et al. (2022) observed that elevated k_t was only observed near the bed due to the jet through the lower gap. These results highlight that the log configuration has a significant impact on the distribution of log-generated k_t.

In addition to the surface flow measurements, Figures S15 and S16 in Supporting Information S1 show the hyporheic flow paths induced by the logs at the above three vertical locations. For single log cases with a log placed near the water surface ($z = 14.5$ cm), midwater depth ($z = 9$ cm), and sediment bed ($z = 4.5$ cm), $L_{H,\text{up}} = 48.8$, 44.0, and 26.0 cm, and $L_{H,\text{down}} = 47.2, 16.0, 41.7$ cm, respectively. This suggests that $L_{H,\text{up}}$ increased with increasing gap ratio. In contrast, $L_{H,\text{down}}$ for the logs placed at $z = 4.5$ and 14.5 cm was three times that of the logs placed at the mid-water depth. For two log cases with the logs placed near the water surface, midwater depth, and sediment bed, $L_{H,\text{up}} = 77.2, 54.0$, and 61.9 cm, and $L_{H,\text{down}} = 41.3, 15.0$, and 35.6 cm, respectively. The hyporheic flow patterns when the logs were placed near the water surface and sediment bed resembled the Stage II and Stage III patterns in Figure 1, respectively. Finally, our results show that the hyporheic flux decreased by 65% when the gap ratio increased by 6 times in both single log cases and two log cases (Figure S17 in Supporting Information S1).

5.4. Limitations of This Study and Future Work

In this study, we investigated the relationship between the surface flow and hyporheic flow around two in-line logs with a simplified configuration. We acknowledge that natural conditions can be more complicated in many ways. First, we conducted our experiments in a rectangular channel. While many natural channels have been approximated as rectangular channels (Manga & Kirchner, 2000), the inclination or meanders of channels can introduce lateral hyporheic flow. Such an effect is not considered here. Second, we simulated natural wood logs using smooth cylinders. We anticipate that the roughness of natural wood would increase drag forces on the surrounding flow, leading to a higher head loss and a higher hyporheic flow rate. Additionally, branches on the natural wood would generate additional eddies and turbulence. These small flow structures may affect the flow patterns, especially when the two logs were placed very close to each other. Finally, we only considered cases with two submerged in-line logs of the same diameter placed at the same vertical location. The head loss due to the logs, flow patterns, and related critical L_{c-c} may change if the logs are not in-line or of the same size (Jiang & Lin, 2012; Sumner, 2010). The angle between the log and the flow direction and the asymmetry of the natural log may also play important roles in inducing hyporheic flow. The impact of the randomness of the wood log arrangement in the field can introduce additional complexity.

6. Conclusions

Here, we quantified the impact of the two in-line logs on both surface flow and hyporheic flow. Our results show that the length scale of the log-induced hyporheic flow increased linearly with the center-to-center distance between two logs (L_{c-c}) if $L_{c-c} \geq 3D$. The hyporheic flux and the water surface difference induced by two in-line logs can be estimated as that of two individual logs when $L_{c-c} > 10D$. We also connected the development stages of the log-induced hyporheic flow pattern with the surface flow regime: Stage I of the hyporheic flow pattern development is related to the surface flow in both the extended-body regime and the reattachment regime ($L_{c-c} < 3D$). Stage II of the hyporheic flow pattern development is related to the surface flow in the transition state between the reattachment regime and the co-shedding regime ($L_{c-c} = 3D$). Stages III and IV of the hyporheic flow pattern development are related to the surface flow in the co-shedding regime ($L_{c-c} > 3D$). To gain the maximum log-induced hyporheic flow rate, our study suggests introducing the logs into the channel with $L_{c-c} > 10D$. Our finding facilitates the knowledge of the hyporheic flow induced by a series of logs and can help in the design of future restoration projects that involve wood reintroduction.

Data Availability Statement

The surface flow velocity measurements, water surface profiles, and dye visualization data for the hyporheic flow, along with the associated processing codes, have been deposited in the Data Repository for the University of Minnesota (Huang & Yang, 2024, https://doi.org/10.13020/erpk-4v14).

Acknowledgments

The research was supported by the National Science Foundation (EAR 2209591). The authors would like to thank Benjamin Erickson for help with the modification of the flume.

References

Ader, E., Wohl, E., McFadden, S., & Singha, K. (2021). Logjams as a driver of transient storage in a mountain stream. *Earth Surface Processes and Landforms*, *46*(3), 701–711. https://doi.org/10.1002/esp.5057

Boano, F., Demaria, A., Revelli, R., & Ridolfi, L. (2010). Biogeochemical zonation due to intrameander hyporheic flow. *Water Resources Research*, *46*(2), W02511. https://doi.org/10.1029/2008wr007583

Boano, F., Harvey, J. W., Marion, A., Packman, A. I., Revelli, R., Ridolfi, L., & Wörman, A. (2014). Hyporheic flow and transport processes: Mechanisms, models, and biogeochemical implications. *Reviews of Geophysics (1985)*, *52*(4), 603–679. https://doi.org/10.1002/2012rg000417

Boulton, A. J., Findlay, S., Marmonier, P., Stanley, E. H., & Valett, H. M. (1998). The functional significance of the hyporheic zone in streams and rivers. *Annual Review of Ecology and Systematics*, *29*(1), 59–81. https://doi.org/10.1146/annurev.ecolsys.29.1.59

Canny, J. (1986). A computational approach to edge detection. *IEEE Transactions on Pattern Analysis and Machine Intelligence*(6), 679–698. https://doi.org/10.1109/tpami.1986.4767851

Chen, W., Ji, C., Xu, D., & Zhang, Z. (2020). Vortex-induced vibrations of two inline circular cylinders in proximity to a stationary wall. *Journal of Fluids and Structures*, *94*, 102958. https://doi.org/10.1016/j.jfluidstructs.2020.102958

Das, B. M. (2021). *Principles of geotechnical engineering*. Cengage learning.

Doughty, M., Sawyer, A., Wohl, E., & Singha, K. (2020). Mapping increases in hyporheic exchange from channel-spanning logjams. *Journal of Hydrology*, *587*, 124931. https://doi.org/10.1016/j.jhydrol.2020.124931

Drummond, J. D., Nel, H. A., Packman, A. I., & Krause, S. (2020). Significance of hyporheic exchange for predicting microplastic fate in rivers. *Environmental Science and Technology Letters*, *7*(10), 727–732. https://doi.org/10.1021/acs.estlett.0c00595

Endreny, T., Lautz, L., & Siegel, D. (2011). Hyporheic flow path response to hydraulic jumps at river steps: Flume and hydrodynamic models. *Water Resources Research*, *47*(2), W02518. https://doi.org/10.1029/2009wr008631

Ensign, S. H., & Doyle, M. W. (2005). In-channel transient storage and associated nutrient retention: Evidence from experimental manipulations. *Limnology & Oceanography*, *50*(6), 1740–1751. https://doi.org/10.4319/lo.2005.50.6.1740

Follett, E., Schalko, I., & Nepf, H. (2020). Momentum and energy predict the backwater rise generated by a large wood jam. *Geophysical Research Letters*, *47*(17), e2020GL089346. https://doi.org/10.1029/2020gl089346

Follett, E., Schalko, I., & Nepf, H. (2021). Logjams with a lower gap: Backwater rise and flow distribution beneath and through logjam predicted by two-box momentum balance. *Geophysical Research Letters*, *48*(16), e2021GL094279. https://doi.org/10.1029/2021gl094279

Gooseff, M. N. (2010). Defining hyporheic zones–advancing our conceptual and operational definitions of where stream water and groundwater meet. *Geography Compass*, *4*(8), 945–955. https://doi.org/10.1111/j.1749-8198.2010.00364.x

Grabowski, R. C., Gurnell, A. M., Burgess-Gamble, L., England, J., Holland, D., Klaar, M. J., et al. (2019). The current state of the use of large wood in river restoration and management. *Water and Environment Journal*, *33*(3), 366–377. https://doi.org/10.1111/wej.12465

Hart, D., Mulholland, P., Marzolf, E., DeAngelis, D., & Hendricks, S. (1999). Relationships between hydraulic parameters in a small stream under varying flow and seasonal conditions. *Hydrological Processes*, *13*(10), 1497–1510. https://doi.org/10.1002/(sici)1099-1085(199907)13:10<1497::aid-hyp825>3.0.co;2-1

Huang, S., & Yang, J. Q. (2022). Impacts of emergent vegetation on hyporheic exchange. *Geophysical Research Letters*, *49*(13), e2022GL099095. https://doi.org/10.1029/2022gl099095

Huang, S. H., & Yang, J. Q. (2023). Impacts of channel-spanning log jams on hyporheic flow. *Water Resources Research*, *59*(11), e2023WR035217. https://doi.org/10.1029/2023wr035217

Huang, S. H., & Yang, J. Q. (2024). Experimental data of the log-induced hyporheic flow experiment in the 6-inch flume of St. Anthony Falls Laboratory in 2023 [Dataset]. *DRUM*. https://doi.org/10.13020/erpk-4v14

Hygelund, B., & Manga, M. (2003). Field measurements of drag coefficients for model large woody debris. *Geomorphology*, *51*(1–3), 175–185. https://doi.org/10.1016/s0169-555x(02)00335-5

Igarashi, T. (1984). Characteristics of the flow around two circular cylinders arranged in tandem: 2nd report, unique phenomenon at small spacing. *Bulletin of JSME*, *27*(233), 2380–2387. https://doi.org/10.1299/jsme1958.27.2380

ISO. (2003). *Measurement of fluid flow by means of pressure differential devices inserted in circular cross-section conduits running full—Part 2: Orifice plates*. Geneva: International Organization for Standardization. ISO 5167-2:2003.

Jaeger, A., Posselt, M., Schaper, J. L., Betterle, A., Rutere, C., Coll, C., et al. (2021). Transformation of organic micropollutants along hyporheic flow in bedforms of river-simulating flumes. *Scientific Reports*, *11*(1), 1–18. https://doi.org/10.1038/s41598-021-91519-2

Janzen, K., & Westbrook, C. J. (2011). Hyporheic flows along a channelled peatland: Influence of beaver dams. *Canadian Water Resources Journal/Revue Canadienne des Ressources Hydriques*, *36*(4), 331–347. https://doi.org/10.4296/cwrj3604846

Jiang, R.-j., & Lin, J.-z. (2012). Wall effects on flows past two tandem cylinders of different diameters. *Journal of Hydrodynamics*, *24*(1), 1–10. https://doi.org/10.1016/s1001-6058(11)60212-6

Keys, T. A., Govenor, H., Jones, C. N., Hession, W. C., Hester, E. T., & Scott, D. T. (2018). Effects of large wood on floodplain connectivity in a headwater Mid-Atlantic stream. *Ecological Engineering*, *118*, 134–142. https://doi.org/10.1016/j.ecoleng.2018.05.007

Khosronejad, A., Hansen, A., Kozarek, J., Guentzel, K., Hondzo, M., Guala, M., et al. (2016). Large eddy simulation of turbulence and solute transport in a forested headwater stream. *Journal of Geophysical Research: Earth Surface*, *121*(1), 146–167. https://doi.org/10.1002/2014jf003423

Lester, R. E., & Boulton, A. J. (2008). Rehabilitating agricultural streams in Australia with wood: A review. *Environmental Management 2008*, *42*(2), 310–326. https://doi.org/10.1007/s00267-008-9151-1

Li, A., Aubeneau, A. F., Bolster, D., Tank, J. L., & Packman, A. I. (2017). Covariation in patterns of turbulence-driven hyporheic flow and denitrification enhances reach-scale nitrogen removal. *Water Resources Research*, *53*(8), 6927–6944. https://doi.org/10.1002/2016wr019949

Ljungkrona, L., Norberg, C., & Sundén, B. (1991). Free-stream turbulence and tube spacing effects on surface pressure fluctuations for two tubes in an in-line arrangement. *Journal of Fluids and Structures*, *5*(6), 701–727. https://doi.org/10.1016/0889-9746(91)90364-u

Ma, L., Shi, Y., Siemianowski, O., Yuan, B., Egner, T. K., Mirnezami, S. V., et al. (2019). Hydrogel-based transparent soils for root phenotyping in vivo. *Proceedings of the National Academy of Sciences*, Vol. 116(22), 11063–11068. https://doi.org/10.1073/pnas.1820334116

Majerova, M., Neilson, B., Schmadel, N., Wheaton, J., & Snow, C. (2015). Impacts of beaver dams on hydrologic and temperature regimes in a mountain stream. *Hydrology and Earth System Sciences*, *19*(8), 3541–3556. https://doi.org/10.5194/hess-19-3541-2015

Manga, M., & Kirchner, J. W. (2000). Stress partitioning in streams by large woody debris. *Water Resources Research*, *36*(8), 2373–2379. https://doi.org/10.1029/2000wr900153

Marion, A., Bellinello, M., Guymer, I., & Packman, A. (2002). Effect of bed form geometry on the penetration of nonreactive solutes into a streambed. *Water Resources Research*, *38*(10), 27-21–12. https://doi.org/10.1029/2001wr000264

Marston, R. A. (1982). The geomorphic significance of log steps in forest Streams[1]. *Annals of the Association of American Geographers*, *72*(1), 99–108. https://doi.org/10.1111/j.1467-8306.1982.tb01386.x

McCallum, J. L., Höhne, A., Schaper, J. L., Shanafield, M., Banks, E. W., Posselt, M., et al. (2020). A numerical stream transport modeling approach including multiple conceptualizations of hyporheic exchange and spatial variability to assess contaminant removal. *Water Resources Research*, *56*(3), e2019WR024987. https://doi.org/10.1029/2019wr024987

Müller, S., Follett, E. M., Ouro, P., & Wilson, C. A. M. E. (2022). Influence of channel-spanning engineered logjam structures on channel hydrodynamics. *Water Resources Research*, *58*(12). https://doi.org/10.1029/2022wr032111

Nagayama, S., & Nakamura, F. (2010). Fish habitat rehabilitation using wood in the world. *Landscape and Ecological Engineering 2009*, *6*(2), 289–305. https://doi.org/10.1007/s11355-009-0092-5

O'Connor, B. L., & Harvey, J. W. (2008). Scaling hyporheic exchange and its influence on biogeochemical reactions in aquatic ecosystems. *Water Resources Research*, *44*(12). https://doi.org/10.1029/2008wr007160

O'Connor, B. L., & Hondzo, M. (2008). Dissolved oxygen transfer to sediments by sweep and eject motions in aquatic environments. *Limnology & Oceanography*, *53*(2), 566–578. https://doi.org/10.4319/lo.2008.53.2.0566

Ozdil, N. F. T., & Akilli, H. (2019). Flow comparison around horizontal single and tandem cylinders at different immersion elevations. *Ocean Engineering*, *189*, 106352. https://doi.org/10.1016/j.oceaneng.2019.106352

Packman, A. I., Brooks, N. H., & Morgan, J. J. (2000). Kaolinite exchange between a stream and streambed: Laboratory experiments and validation of a colloid transport model. *Water Resources Research*, *36*(8), 2363–2372. https://doi.org/10.1029/2000wr900058

Parker, C., Henshaw, A. J., Harvey, G. L., & Sayer, C. D. (2017). Reintroduced large wood modifies fine sediment transport and storage in a lowland river channel. *Earth Surface Processes and Landforms*, *42*(11), 1693–1703. https://doi.org/10.1002/esp.4123

Roche, K., Blois, G., Best, J., Christensen, K., Aubeneau, A., & Packman, A. (2018). Turbulence links momentum and solute exchange in coarse-grained streambeds. *Water Resources Research*, *54*(5), 3225–3242. https://doi.org/10.1029/2017wr021992

Roni, P., Beechie, T., Pess, G., & Hanson, K. (2015). Wood placement in river restoration: Fact, fiction, and future direction. *Canadian Journal of Fisheries and Aquatic Sciences*, *72*(3), 466–478. https://doi.org/10.1139/cjfas-2014-0344

Sawyer, A. H., Bayani Cardenas, M., & Buttles, J. (2011). Hyporheic exchange due to channel-spanning logs. *Water Resources Research*, *47*(8). https://doi.org/10.1029/2011wr010484

Sawyer, A. H., Bayani Cardenas, M., & Buttles, J. (2012). Hyporheic temperature dynamics and heat exchange near channel-spanning logs. *Water Resources Research*, *48*(1). https://doi.org/10.1029/2011wr011200

Schalko, I., Wohl, E., & Nepf, H. M. (2021). Flow and wake characteristics associated with large wood to inform river restoration. *Scientific Reports*, *11*(1), 1–12. https://doi.org/10.1038/s41598-021-87892-7

Schaper, J. L., Posselt, M., Bouchez, C., Jaeger, A., Nuetzmann, G., Putschew, A., et al. (2019). Fate of trace organic compounds in the hyporheic zone: Influence of retardation, the benthic biolayer, and organic carbon. *Environmental Science & Technology*, *53*(8), 4224–4234. https://doi.org/10.1021/acs.est.8b06231

Sear, D., Millington, C., Kitts, D., & Jeffries, R. (2010). Logjam controls on channel: Floodplain interactions in wooded catchments and their role in the formation of multi-channel patterns. *Geomorphology*, *116*(3–4), 305–319. https://doi.org/10.1016/j.geomorph.2009.11.022

Spreitzer, G., Tunnicliffe, J., & Friedrich, H. (2021). Effects of large wood (LW) blockage on bedload connectivity in the presence of a hydraulic structure. *Ecological Engineering*, *161*, 106156. https://doi.org/10.1016/j.ecoleng.2021.106156

Stonedahl, S. H., Harvey, J. W., Detty, J., Aubeneau, A., & Packman, A. I. (2012). Physical controls and predictability of stream hyporheic flow evaluated with a multiscale model. *Water Resources Research*, *48*(10). https://doi.org/10.1029/2011wr011582

Sumner, D. (2010). Two circular cylinders in cross-flow: A review. *Journal of Fluids and Structures*, *26*(6), 849–899. https://doi.org/10.1016/j.jfluidstructs.2010.07.001

Swanson, T. E., & Cardenas, M. B. (2010). Diel heat transport within the hyporheic zone of a pool-riffle-pool sequence of a losing stream and evaluation of models for fluid flux estimation using heat. *Limnology & Oceanography*, *55*(4), 1741–1754. https://doi.org/10.4319/lo.2010.55.4.1741

Thielicke, W., & Sonntag, R. (2021). Particle image Velocimetry for MATLAB: Accuracy and enhanced algorithms in PIVlab. *Journal of Open Research Software*, *9*(1), 12. https://doi.org/10.5334/jors.334

Tseng, C. Y., & Tinoco, R. O. (2022). From substrate to surface: A turbulence-based model for gas transfer across sediment-water-air interfaces in vegetated streams. *Water Resources Research*, *58*(1), e2021WR030776. https://doi.org/10.1029/2021wr030776

Voermans, J. J., Ghisalberti, M., & Ivey, G. N. (2018). A model for mass transport across the sediment-water interface. *Water Resources Research*, *54*(4), 2799–2812. https://doi.org/10.1002/2017wr022418

Wallerstein, N. P., Alonso, C. V., Bennett, S. J., & Thorne, C. R. (2002). Surface wave forces acting on submerged logs. *Journal of Hydraulic Engineering*, *128*(3), 349–353. https://doi.org/10.1061/(asce)0733-9429(2002)128:3(349)

Wilhelmsen, K., Sawyer, A., Marshall, A., McFadden, S., Singha, K., & Wohl, E. (2021). Laboratory flume and numerical modeling experiments show log jams and branching channels increase hyporheic exchange. *Water Resources Research*, *57*(9), e2021WR030299. https://doi.org/10.1029/2021wr030299

Wohl, E. (2016). Spatial heterogeneity as a component of river geomorphic complexity. *Progress in Physical Geography*, *40*(4), 598–615. https://doi.org/10.1177/0309133316658615

Wohl, E., Bledsoe, B. P., Fausch, K. D., Kramer, N., Bestgen, K. R., & Gooseff, M. N. (2016). Management of large wood in streams: An overview and proposed framework for hazard evaluation. *Journal of the American Water Resources Association*, *52*(2), 315–335. https://doi.org/10.1111/1752-1688.12388

Wohl, E., & Scamardo, J. E. (2021). The resilience of logjams to floods. *Hydrological Processes*, *35*(1), e13970. https://doi.org/10.1002/hyp.13970

Wohl, E., & Scott, D. N. (2017). Wood and sediment storage and dynamics in river corridors. *Earth Surface Processes and Landforms*, *42*(1), 5–23. https://doi.org/10.1002/esp.3909

Yang, J. Q. (2024). Solute flow and particle transport in aquatic ecosystems: A review on the effect of emergent and rigid vegetation. *Environmental Science and Ecotechnology*, *21*, 100429. https://doi.org/10.1016/j.ese.2024.100429

Zhang, N., Rutherfurd, I., & Ghisalberti, M. (2020). Effect of instream logs on bank erosion potential: A flume study with a single log. *Journal of Ecohydraulics*, *5*(1), 43–56. https://doi.org/10.1080/24705357.2019.1634499

Zhou, Y., & Yiu, M. (2006). Flow structure, momentum and heat transport in a two-tandem-cylinder wake. *Journal of Fluid Mechanics*, *548*, 17–48. https://doi.org/10.1017/s002211200500738x